

# The Impact of Molecular Hydrogen Cooling on the Galaxy Formation Threshold

ETHAN O. NADLER<sup>1</sup>

<sup>1</sup>*Department of Astronomy & Astrophysics, University of California, San Diego, La Jolla, CA 92093, USA*

## ABSTRACT

We study the impact of molecular (H<sub>2</sub>) and atomic (H I) hydrogen cooling on the galaxy formation threshold. We calculate the fraction of dark matter (DM) halos that exceed a critical mass required for star formation,  $M_{\text{crit}}(z)$ , as a function of their peak mass. By convolving analytic halo mass accretion histories (MAHs) with models for  $M_{\text{crit}}(z)$ , we predict that halos with peak virial masses below  $\sim 10^8 M_{\odot}$  can form stars before reionization through H<sub>2</sub> cooling. These halos remain dark when only H I cooling and reionization are modeled. However, less than  $\approx 10\%$  of halos with peak masses below  $\sim 10^7 M_{\odot}$  ever exceed  $M_{\text{crit}}(z)$ , even when H<sub>2</sub> cooling is included; this threshold is primarily set by relative streaming motion between DM and baryons imprinted at recombination. We obtain similar results using subhalo MAHs from an extremely high-resolution cosmological DM-only zoom-in simulation of a Milky Way (MW) analog (particle mass  $6.3 \times 10^3 M_{\odot}$ ). Based on the abundance of MW satellites, these results imply that at least some known ultra-faint dwarf galaxies formed through H<sub>2</sub> cooling. This work sharpens predictions for the galaxy formation threshold and demonstrates how its essential features emerge from the underlying distribution of halo growth histories.

*Keywords:* Galaxy formation (595); Star formation (1569); Galaxy dark matter halos (1880)

## 1. INTRODUCTION

What is the halo mass threshold for galaxy formation? This question underlies key areas of research in galaxy formation and cosmology, including when and how the first galaxies formed, which galaxies drive cosmic reionization, and whether “dark” (galaxy-free) dark matter (DM) halos exist. Robust predictions for the galaxy formation threshold are critical given upcoming observations of faint galaxies and low-mass halos throughout cosmic history (e.g., see Bechtol et al. 2022 and Robertson 2022 for reviews).

The physics that regulates galaxy formation in low-mass halos is well studied. Molecular hydrogen (H<sub>2</sub>) cooling enables star formation in  $\sim 10^6 M_{\odot}$  ‘minihalos’ before reionization ( $z \gtrsim 10$ ; Haiman et al. 1996; Tegmark et al. 1997). Hydrodynamic simulations indicate that H<sub>2</sub> cooling is partially—but not entirely—suppressed by Lyman-Werner (LW) background radiation at these redshifts (e.g., Machacek et al. 2001; Abel et al. 2002; Wise & Abel 2007). Meanwhile, atomic hydrogen (H I) is the main coolant in halos with masses above  $\sim 10^8 M_{\odot}$ , or virial temperatures above  $\sim 10^4$  K, before reionization (Greif et al. 2008). Reionization subsequently heats the intergalactic medium (IGM), raising the minimum halo mass for star formation above  $\sim 10^9 M_{\odot}$  at  $z \lesssim 5$  (Efstathiou 1992; Barkana & Loeb 1999).

Translating these processes into a prediction for which halos host galaxies across cosmic time remains challenging.

Before reionization, halos more massive than the H I cooling limit are expected to form stars (Greif et al. 2008). However, H<sub>2</sub> cooling can occur in halos above and below this limit, with an efficiency set by the local, time-dependent LW background (e.g., Haiman et al. 1997; Oh & Haiman 2002; O’Shea & Norman 2008). The first galaxies drive reionization, which sets the star formation threshold at later times (e.g., Wise et al. 2014; Norman et al. 2018). Cosmological hydrodynamic simulations are needed to capture how Population III star formation, external enrichment and metal-line cooling, self-shielding, cold-mode accretion, supernova feedback, and DM–baryon streaming affect this picture (e.g., Wise et al. 2012; Jaacks et al. 2019; Liu & Bromm 2020; Skinner & Wise 2020; Kulkarni et al. 2021; Munshi et al. 2021; Schauer et al. 2019, 2021; Hicks et al. 2021, 2024).

Despite this complexity, several recent studies predict a global, time-dependent halo mass threshold for star formation,  $M_{\text{crit}}(z)$ , by combining analytic calculations and semi-analytic models fit to hydrodynamic simulations. Specifically, Nebrin, Giri, & Mellema (2023, hereafter NGM23) modeled the impact of H<sub>2</sub> and H I cooling on the galaxy formation threshold, accounting for LW radiation, self-shielding, reionization, and DM–baryon streaming; also see Hegde & Furlanetto (2023, hereafter HF23). Meanwhile, Benitez-Llambay & Frenk (2020, hereafter BF20) focused on the effects of H I cooling and reionization without modeling H<sub>2</sub> cooling. BF20 convolved their model for  $M_{\text{crit}}(z)$  with halo mass accretion histories (MAHs) from extended Press–Schechter (ePS) theory and cosmological simulations

to predict the galaxy occupation fraction,  $f_{\text{gal}}$ : the fraction of DM halos that host galaxies as a function of halo mass.

Herein, we model the impact of  $\text{H}_2$  and  $\text{H}\text{I}$  cooling on the galaxy formation threshold, focusing on the lowest-mass halos that form stars before reionization. Unlike previous work, we predict  $f_{\text{gal}}$  using models for  $M_{\text{crit}}(z)$  with and without  $\text{H}_2$  cooling and DM–baryon streaming. We apply our model to both isolated halos, using analytic MAHs, and subhalos, using MAHs from a high-resolution cosmological zoom-in simulation of a Milky Way (MW) analog. Throughout, we demonstrate how  $f_{\text{gal}}$  arises from the underlying distribution of halo growth histories.

These predictions are timely in light of upcoming data. The Vera C. Rubin Observatory (Ivezic et al. 2019) will discover hundreds of new dwarf galaxies, improving constraints on the faint-end galaxy–halo connection (Nadler et al. 2024). Predictions for  $f_{\text{gal}}$  in various galaxy formation scenarios will be needed to accurately interpret these observations. In parallel, strong gravitational lensing is beginning to probe (sub)halos that may remain dark (see Vegetti et al. 2023 for a review). A detection of “dark” halos using strong lensing will thus require a thorough understanding of the galaxy formation threshold itself.

This letter is organized as follows. In Section 2, we describe our  $M_{\text{crit}}(z)$  and isolated halo MAH models, and our procedure for calculating  $f_{\text{gal}}$ . We predict  $f_{\text{gal}}$  for isolated halos in Section 3 and for MW subhalos in Section 4. We summarize and discuss our results in Section 5. We define halo masses using the Bryan & Norman (1998) virial overdensity and adopt cosmological parameters  $h = 0.7$ ,  $\Omega_{\text{m}} = 0.286$ ,  $\Omega_{\text{b}} = 0.047$ , and  $\Omega_{\Lambda} = 0.714$  (Hinshaw et al. 2013).

## 2. MODEL

### 2.1. Critical Halo Mass for Star Formation

We use  $M_{\text{crit}}(z)$  from **NGM23** and **BF20** as our fiducial star formation thresholds with and without  $\text{H}_2$  cooling, respectively. We apply a symmetric, redshift-independent scatter of  $\sigma_{\log(M)} = 0.2$  dex to each of these global  $M_{\text{crit}}(z)$  histories. This value is comparable to the intrinsic scatter in  $M_{\text{crit}}(z)$  measured from small-volume ( $\lesssim 1$  Mpc  $h^{-1}$ ) hydrodynamic simulations using a uniform LW background (Kulkarni et al. 2021). Figure 1 shows both  $M_{\text{crit}}(z)$  models (solid blue and orange lines and bands), along with the  $\text{H}_2$  and  $\text{H}\text{I}$  cooling-only limits from **NGM23** (dashed blue and orange lines).

We implement the **NGM23** model as follows. We choose a fiducial DM–baryon streaming velocity of  $v_{\text{str}}(z) = \sigma_{\text{str}}(z)$ , where  $\sigma_{\text{str}}(z)$  is the global root–mean–square value (Tseliakhovich & Hirata 2010; Fialkov et al. 2012). We make this choice because the streaming velocity follows a Maxwellian distribution with a most probable value of  $0.82\sigma_{\text{str}}(z)$  (see **HF23**). Based on the properties of MW satellites and metal-poor stars in the MW stellar halo, Uysal & Hartwig (2023) inferred  $v_{\text{str}}(z) \gtrsim \sigma_{\text{str}}(z)$  locally; we study the effects of varying  $v_{\text{str}}(z)$  in Appendix A. Following **NGM23**, we use the photoionization history from Faucher-Giguère (2020) and the LW background from Incatasciato et al. (2023), such that  $\text{H}\text{I}$  is reionized by  $z \approx 7$ . Note that LW radiation does not in-

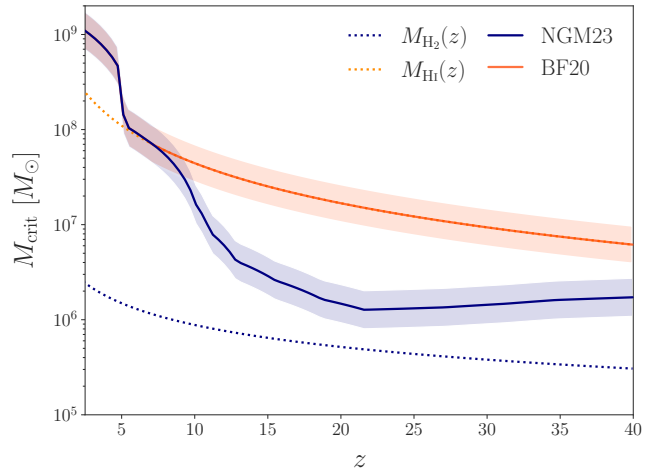


**Figure 1.** Halo mass thresholds for star formation. The thick blue line (which includes  $\text{H}_2$  cooling) shows our fiducial **NGM23** model with DM–baryon streaming velocity  $v_{\text{str}}(z) = \sigma_{\text{str}}(z)$ . The thick orange line (which does not include  $\text{H}_2$  cooling) shows our fiducial **BF20** model with  $z_{\text{reion}} = 7$ . Shaded bands show the assumed 0.2 dex scatter in  $\log(M_{\text{crit}}(z))$ .  $\text{H}_2$  and  $\text{H}\text{I}$  cooling-only limits from **NGM23** are shown by dotted blue and orange lines, respectively.

stantly heat self-shielded gas in halos at high redshifts; thus,  $M_{\text{crit}}(z)$  increases rapidly at  $z \approx 5$  in our **NGM23** implementation. The **NGM23** model we adopt does not include metal-line cooling or dust-catalyzed  $\text{H}_2$  formation, which these authors conclude negligibly affect  $M_{\text{crit}}(z)$ .

**BF20** assumed that  $\text{H}\text{I}$  cooling sets  $M_{\text{crit}}(z)$  before reionization and that the IGM is then instantaneously heated to  $2 \times 10^4$  K, such that  $M_{\text{crit}}(z)$  is set by the corresponding virial temperature threshold afterward. Thus, a relevant free parameter in **BF20** is the reionization redshift,  $z_{\text{reion}}$ . We set  $z_{\text{reion}} = 7$  and match  $M_{\text{crit}}(z)$  to **NGM23** for  $z < z_{\text{reion}}$ . Figure 1 shows that our **BF20**  $M_{\text{crit}}(z)$  model matches the  $\text{H}\text{I}$  cooling limit before reionization and matches our **NGM23** model after. We refer the reader to **BF20** for a study of how varying  $z_{\text{reion}}$  affects  $f_{\text{gal}}$  predictions in this model.

### 2.2. Halo Mass Accretion Histories

We model isolated halo MAHs via (Wechsler et al. 2002)

$$\begin{aligned} M(z|M_{\text{o}}, z_{\text{o}}) &= M_{\text{o}} \exp \left[ -\frac{S c_1}{c_{\text{o}}(1+z_{\text{o}})} \left( \frac{1+z}{1+z_{\text{o}}} - 1 \right) \right] \\ &= M_{\text{o}} \exp \left[ -\frac{S c_1}{c_{\text{o}}} \frac{z-z_{\text{o}}}{(1+z_{\text{o}})^2} \right], \end{aligned} \quad (1)$$

where  $M_{\text{o}} \equiv M(z_{\text{o}})$  is the halo mass at redshift  $z_{\text{o}}$ ,  $S = 2$ ,  $c_1 = 4.2$  is the virial concentration of a typical halo collapsing today, and  $c_{\text{o}}$  is the concentration at  $z_{\text{o}}$ . While Equation 1 was not explicitly calibrated to simulations over the mass and redshift range we study, it provides simple and powerful predictions that are sufficient to capture key features of the galaxy formation threshold. This model has been refined in subsequent work (e.g., van den Bosch et al. 2014), and we leave a detailed exploration of such MAH models to future work.

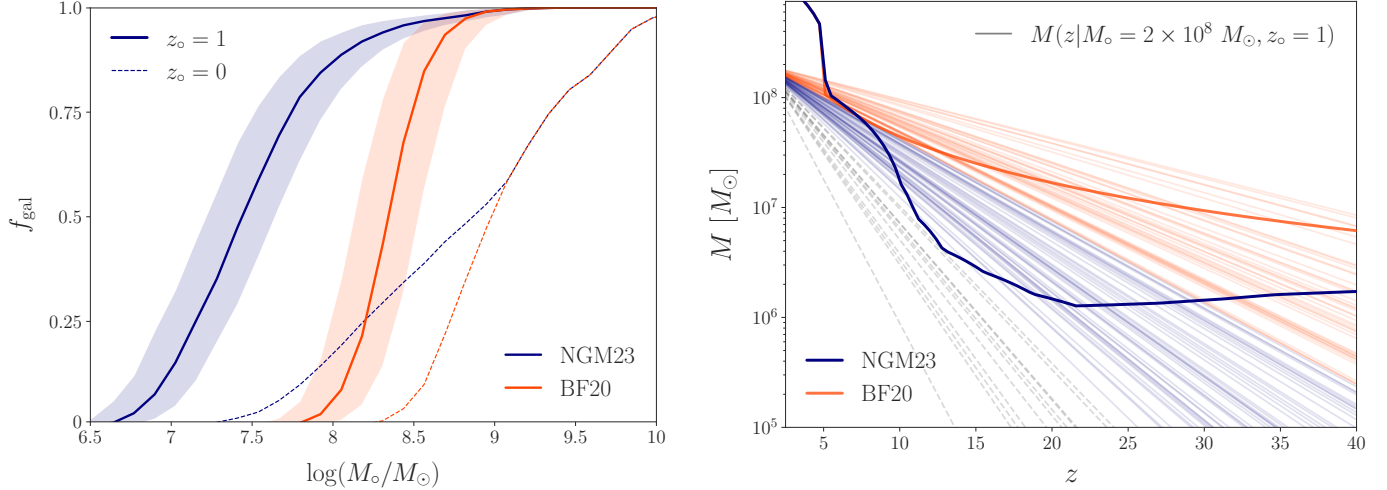


**Figure 2.** *Left:* Median galaxy occupation fraction for isolated halos as a function of halo mass at  $z_0 = 1$  (solid) and  $z_0 = 0$  (dashed), generated by combining analytic MAHs with  $M_{\text{crit}}(z)$  from **NGM23** (blue) or **BF20** (orange). Shaded bands show 16% to 84% intrinsic scatter quantiles. *Right:* Halo growth histories. Thin lines show MAHs with  $z_0 = 1$  and  $M_0 = 2 \times 10^8 M_\odot$ , colored according to whether they exceed the mean  $M_{\text{crit}}(z)$  from **BF20** (orange), **NGM23** (blue), or neither (dashed gray). Thick lines show the  $M_{\text{crit}}(z)$  models.

To generate MAHs, we sample  $c_0$  from the Diemer & Joyce (2019) mass–concentration relation at  $z_0$  with a redshift-independent scatter of  $\sigma_{\log(c)} = 0.16$  dex. We study the effects of varying  $\sigma_{\log(c)}$  in Appendix B.

### 2.3. Galaxy Occupation Fraction

We define the galaxy occupation as follows:

$$f_{\text{gal}}(M_0, z_0) \equiv \int d\Delta [p(\Delta) \times p(\exists z \in [z_{\text{min}}, z_{\text{max}}] : \log(M(z|M_0, z_0)) > \log(M_{\text{crit}}(z)) + \Delta)], \quad (2)$$

where we marginalize over scatter in  $\log(M_{\text{crit}}(z))$  by drawing from  $p(\Delta)$  as described in each section below. We set  $z_{\text{max}} = 40$  and do not model star formation at earlier times. Note that DM–baryon streaming causes  $M_{\text{crit}}(z)$  to increase for  $z \gtrsim 20$  in our fiducial **NGM23** model; as a result, our predictions in this case are not sensitive to  $z_{\text{max}}$ , so long as  $z_{\text{max}} \gtrsim 20$ . We set  $z_{\text{min}} = z_0$ ; increasing  $z_{\text{min}}$  does not significantly affect our predictions, so long as  $z_{\text{min}} < z_{\text{reion}}$ , because  $M_{\text{crit}}(z)$  increases sharply at reionization in both  $M_{\text{crit}}(z)$  models we consider.

According to Equation 2, the fraction of halos that host galaxies is equal to the probability that their MAHs exceed  $M_{\text{crit}}(z)$  between  $z_0$  and  $z_{\text{max}} > z_0$ . Thus, we effectively assume that halos which exceed  $M_{\text{crit}}(z)$  for any amount of time form and retain stars. This assumption is simplistic, since star formation is not instantaneous or permanent. Nonetheless, we will show that our predictions broadly agree with more detailed semi-analytic models, suggesting that Equation 2 captures the key physics that sets  $f_{\text{gal}}$ .

## 3. PREDICTIONS FOR ISOLATED HALOS

To calculate  $f_{\text{gal}}$  for isolated halos, we generate MAHs in bins of  $\log(M_0/M_\odot)$  and marginalize over  $\Delta$  in each bin

by drawing from a normal distribution  $\mathcal{N}(\mu = 0, \sigma = \sigma_{\log(M)})$ . Thus, we predict both the mean  $f_{\text{gal}}$  and its intrinsic scatter. We do not model cosmic variance due to large-scale fluctuations in the photoionization history or LW background.

The left panel of Figure 2 shows our  $f_{\text{gal}}$  predictions for isolated halos with  $z_0 = 0$  (dashed) and  $z_0 = 1$  (solid) using the **NGM23** (blue) and **BF20** (orange)  $M_{\text{crit}}(z)$  models. We predict that halos with  $M(z=0) \gtrsim 10^{8.5} M_\odot$  form stars through H<sub>I</sub> cooling, in agreement with **BF20** (see their Figure 11). Meanwhile, halos with  $10^{7.5} M_\odot \lesssim M(z=0) \lesssim 10^{8.5} M_\odot$  can form stars through H<sub>2</sub> cooling. For  $z_0 = 1$ , H<sub>I</sub> cooling enables star formation for  $M(z=1) \gtrsim 10^8 M_\odot$  halos, while H<sub>2</sub> cooling enables star formation for  $10^7 M_\odot \lesssim M(z=1) \lesssim 10^8 M_\odot$ .<sup>1</sup> The resulting lower limits are primarily set by DM–baryon streaming, which causes the **NGM23**  $M_{\text{crit}}(z)$  model shown in Figure 1 to flatten at high redshifts.

At fixed  $M_0$ , increasing  $z_0$  raises  $f_{\text{gal}}$  because it forces halos to achieve a given mass earlier, resulting in even larger masses at later times. When varying  $z_0$ , our  $f_{\text{gal}}$  predictions are connected by the underlying distribution of halo MAHs, which is not linear in  $z_0$ . As a result, changing  $z_0$  alters the slope of  $f_{\text{gal}}$  in addition to shifting it horizontally. In the  $z_0 = 0$  case, MAHs along the  $f_{\text{gal}}$  cutoff intersect the rapidly-rising part of our  $M_{\text{crit}}(z)$  models near reionization, yielding a sharper feature in  $f_{\text{gal}}$ ; meanwhile, in the  $z_0 = 1$  case, MAHs cross  $M_{\text{crit}}(z)$  in a regime where it is roughly constant in the **NGM23** case. In Appendix C, we derive the error function-like shape of  $f_{\text{gal}}$  analytically under certain assumptions.

Including H<sub>2</sub> cooling allows lower-mass halos to form stars and yields a shallower occupation fraction. To illustrate how this arises, the right panel of Figure 2 shows isolated halo

<sup>1</sup> Note that  $z_0 = 1$  corresponds to the redshift at which typical MW subhalos reach their peak mass (Kazuno et al. 2024).

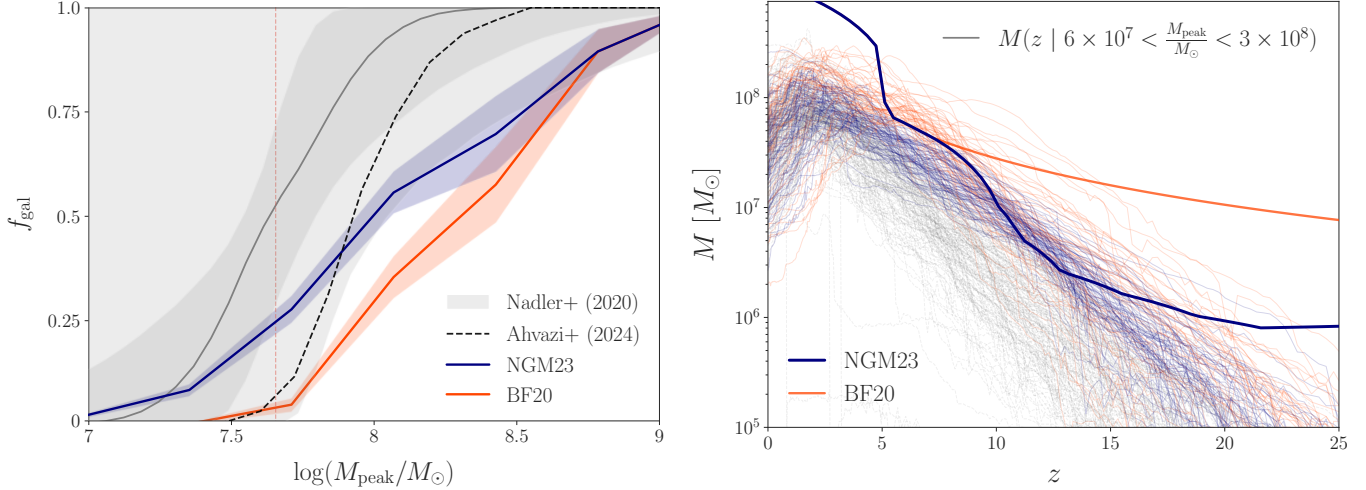


**Figure 3.** *Left:* Median galaxy occupation fraction for MW subhalos predicted using our MW analog simulation. Results are shown using the NGM23 (blue) and BF20 (orange)  $M_{\text{crit}}(z)$  models. Shaded bands show 16% to 84% quantiles from bootstrap resampling. Dark (light) gray bands show the 68% (95%) confidence  $f_{\text{gal}}$  MW satellite posterior from Nadler et al. (2020); the thin gray line shows the median and the dotted vertical red line shows the resolution limit from that study. The dashed black line shows  $f_{\text{gal}}$  from the Ahvazi et al. (2024) semi-analytic model, which includes  $\text{H}_2$  cooling. *Right:* MAHs for subhalos with  $6 \times 10^7 M_{\odot} < M_{\text{peak}} < 3 \times 10^8 M_{\odot}$ , colored according to whether they exceed  $M_{\text{crit}}$  from BF20 (orange), NGM23 (blue), or neither (dashed gray), where both  $M_{\text{crit}}(z)$  models have been decreased by  $\sigma_{\log(M)}$ .

MAHs with  $M_{\odot} = 2 \times 10^8 M_{\odot}$  and  $z_{\odot} = 1$ , where  $f_{\text{gal}}$  decreases rapidly when using the BF20  $M_{\text{crit}}(z)$  model and much more slowly in the NGM23 case. At this mass, the halos that exceed  $M_{\text{crit}}(z)$  from BF20 are high-concentration objects that form early (Wechsler et al. 2002). As  $M_{\odot}$  decreases, MAHs decrease roughly linearly at all times according to Equation 1, but concentration only rises slowly ( $c \sim M^{-0.1}$  or shallower; Correa et al. 2015). Thus, when using a lower  $M_{\text{crit}}(z)$  threshold due to  $\text{H}_2$  cooling, we find a population of halos that exceed  $M_{\text{crit}}(z)$  from NGM23 but not from BF20.

#### 4. PREDICTIONS FOR MILKY WAY SUBHALOS

To predict  $f_{\text{gal}}$  for MW subhalos in a cosmological setting, we run a DM-only zoom-in resimulation of a host from the Milky Way-est suite (Buch et al. 2024). Specifically, we resimulate Halo004 with six MUSIC (Hahn & Abel 2011) refinement regions, a high-resolution particle mass of  $6.3 \times 10^3 M_{\odot}$ , and a Plummer-equivalent gravitational softening of  $40 \text{ pc } h^{-1}$ . This host forms in a large-scale underdensity, decreasing the expected strength of the LW background and thus  $M_{\text{crit}}(z)$  at its location (Kulkarni et al. 2021; Incatasciato et al. 2023). At  $z = 0$ , the host’s virial mass is  $1.03 \times 10^{12} M_{\odot}$  and it contains a  $1.5 \times 10^{11} M_{\odot}$  LMC analog, which accretes at  $z = 0.09$  (lookback time 1.3 Gyr) and reaches a pericentric distance of 59 kpc today. We save a large number of output snapshots starting at  $z = 99$ , and we generate halo catalogs and merger trees using ROCKSTAR and CONSISTENT-TREES (Behroozi et al. 2013a,b).

From this simulation, we use the main-branch MAHs of all surviving subhalos with  $M(z = 0) > 1.9 \times 10^6 M_{\odot}$ , yield-

ing 2930 total subhalos.<sup>2</sup> We measure  $f_{\text{gal}}$  as a function of peak mass before infall into any host,  $M_{\text{peak}} \equiv \max(M(z > z_{\text{infall}}))$ . To assess statistical uncertainties, we resample subhalos in each  $\log(M_{\text{peak}}/M_{\odot})$  with replacement. Rather than marginalizing over intrinsic scatter as in Section 3, we calculate uncertainties by bootstrap resampling the simulated MAHs, which are dominant for statistically-limited comparisons to observed MW satellites. To account for the underdense environment of our MW analog, we decrease  $\log(M_{\text{crit}}(z))$  by  $\sigma_{\log(M)}$  in both  $M_{\text{crit}}(z)$  models, i.e., we set  $p(\Delta) = \delta(\Delta + 0.2)$ . We comment on this choice below.

Our high-resolution resimulation is necessary to capture the  $f_{\text{gal}}$  cutoff, which is sensitive to the MAHs of halos with peak masses above  $\approx 10^7 M_{\odot}$  when  $\text{H}_2$  cooling is included. We resolve such subhalos with thousands of particles at first infall, and their progenitors are typically resolved with  $\gtrsim 100$  particles (corresponding to masses of  $\approx 10^6 M_{\odot}$ ) up to  $z \approx 20$ . Our  $M_{\text{crit}}(z)$  models enable star formation in halo masses above  $\approx 2 \times 10^6 M_{\odot}$  at these redshifts, implying that our resolution is sufficient. We confirm this argument by showing that our  $f_{\text{gal}}$  predictions converge in Appendix D.

The left panel of Figure 3 shows the resulting  $f_{\text{gal}}$  predictions for MW subhalos using the NGM23 (blue) and BF20 (orange)  $M_{\text{crit}}(z)$  models. We predict that  $\text{H}_2$  cooling enables star formation in subhalos with  $10^7 M_{\odot} \lesssim M_{\text{peak}} \lesssim 10^8 M_{\odot}$ ; again, the lower limit is primarily set by DM-baryon streaming. These systems remain dark when only  $\text{H I}$  cooling and reionization are modeled, consistent with our isolated halo results in Figure 2. The NGM23 and BF20 predictions con-

<sup>2</sup> We find that the present-day subhalo mass function is converged above this 300-particle limit, consistent with Nadler et al. (2023).



verge at high  $M_{\text{peak}}$  because our  $M_{\text{crit}}(z)$  models match each other after reionization.

Our  $f_{\text{gal}}$  prediction for MW subhalos is similar to our isolated halo result with  $z_{\circ} = 1$  when using the **BF20** model, but the cutoff shifts toward higher masses by  $\approx 1$  dex in the **NGM23** case. This shift persists when  $z_{\circ}$  in the isolated halo calculation is sampled from our subhalos'  $z_{\text{peak}}$  distribution. The difference results from a relatively low abundance of subhalos with  $10^6 M_{\odot} \lesssim M \lesssim 10^7 M_{\odot}$  at  $z \gtrsim 10$ , as shown by the MAHs in the right panel of Figure 3. This is not a resolution artifact, since we resolve even lower-mass halos at these redshifts. We study host-to-host variance in  $f_{\text{gal}}$  using lower-resolution simulations in Appendix E, finding that this shift may partly be a statistical fluctuation associated with our particular MW analog. The discrepancy may simply indicate that the analytic MAH model does not accurately describe our subhalos' MAH distribution prior to infall, as suggested by comparing the right panels of Figures 2 and 3. Alternatively,  $M_{\text{crit}}(z)$  may fluctuate downward by more than  $\sigma_{\log(M)}$  in the large-scale underdensity inhabited by our MW analog. For example, the 50% occupation mass shifts from  $\sim 10^8 M_{\odot}$  to  $10^{7.75} M_{\odot}$  ( $10^{8.5} M_{\odot}$ ) when  $\Delta = -0.4$  ( $\Delta = 0$ ) is used rather than  $\Delta = -0.2$  in the **NGM23** case. By fixing  $\Delta = -0.2$ , we have assumed that  $M_{\text{crit}}(z)$  decreases by an amount comparable to its intrinsic scatter in the underdense environment of our MW analog. It will be important to refine this assumption both theoretically, in order to self-consistently capture the correlation between subhalo MAHs in a given environment and the large-scale LW background, and observationally, by incorporating constraints on the photoionization history and LW background in the local universe.

We compare our results to  $f_{\text{gal}}$  from the Ahvazi et al. (2024) semi-analytic model, which combines ePS merger trees with a galaxy formation model that includes H<sub>2</sub> cooling but does not include DM–baryon streaming (see the dashed black line in the left panel of Figure 3). Our predicted 50% occupation mass using the **NGM23** model differs from Ahvazi et al. (2024) by only  $\approx 0.1$  dex, although our  $f_{\text{gal}}$  prediction is shallower than theirs. This difference in slope may indicate a larger spread in our subhalos' MAHs, which is expected given that our subhalos form in a cosmological environment and are stripped before entering the host, causing their MAHs to deviate from semi-analytic predictions based on ePS merger trees. Building pre-infall evolution into semi-analytic models will clarify the impact of this effect.

Finally, we compare to the  $f_{\text{gal}}$  posterior from Nadler et al. (2020), which was inferred by forward-modeling the MW satellite population observed by the Dark Energy Survey and Pan-STARRS1 (Drlica-Wagner et al. 2020). Our prediction that includes H<sub>2</sub> cooling and DM–baryon streaming is consistent with Nadler et al. (2020) at the  $2\sigma$  level, while the case that only includes H<sub>I</sub> cooling and reionization is inconsistent with Nadler et al. (2020) for  $M_{\text{peak}} \lesssim 10^{8.5} M_{\odot}$ . These results imply that at least some known ultra-faint MW satellites formed through H<sub>2</sub> cooling and hint that star formation is even more efficient than in **NGM23**; we discuss potential explanations below.

## 5. DISCUSSION AND OUTLOOK

We have shown that H<sub>2</sub> cooling and DM–baryon streaming decrease the peak mass of the smallest halos that can form stars from  $\sim 10^8 M_{\odot}$  to  $\sim 10^7 M_{\odot}$ . This conclusion follows from two basic features of our model: (i) at early times, the halo mass threshold for star formation is  $\sim 2 \times 10^6 M_{\odot}$  when H<sub>2</sub> cooling and DM–baryon streaming are included, and (ii) typical minihalos then grow by  $\sim 1$  dex in mass. Conversely, we predict a lower limit of  $\sim 10^7 M_{\odot}$  on the peak halo mass of any galaxy that is primarily set by DM–baryon streaming.

These conclusions are fairly robust to our choice of semi-analytic  $M_{\text{crit}}(z)$  model, provided that H<sub>2</sub> cooling and DM–baryon streaming are included. To illustrate this, we consider the **HF23** model for  $M_{\text{crit}}(z)$ , which shares many features with **NGM23** but (i) includes X-ray feedback and (ii) does not include reionization.<sup>3</sup> Despite these differences, these authors'  $M_{\text{crit}}(z)$  predictions are in broad agreement. In detail, **HF23** found that X-ray feedback lowers  $M_{\text{crit}}(z)$  relative to **NGM23** by  $\approx 20\%$  at  $z \lesssim 15$  because it photoionizes the IGM and catalyzes H<sub>2</sub> formation. Thus, including X-ray feedback may enable star formation in slightly lower-mass halos than we populate. Meanwhile, **HF23** predicted a rise in  $M_{\text{crit}}(z)$  similar to **NGM23** at  $z \approx 5$  due to LW feedback.

Meanwhile, cosmological hydrodynamic simulations reveal effects beyond those captured in existing semi-analytic models for  $M_{\text{crit}}(z)$ . For example, Kulkarni et al. (2021) and Schauer et al. (2019, 2021) presented simulations including LW radiation and/or DM–baryon streaming. With both effects included, these studies measured  $M_{\text{crit}}(z) \approx 10^6 M_{\odot}$  at  $z \approx 20$ , comparable to our **NGM23** model. Kulkarni et al. (2021) also showed that the effects of LW radiation and DM–baryon streaming on  $M_{\text{crit}}(z)$  are not independent. Semi-analytic models for  $M_{\text{crit}}(z)$  do not capture such correlations, which may impact the environmental dependence of  $f_{\text{gal}}$ . Other hydrodynamic simulations predict efficient hydrogen deuteride (HD) cooling in halos below the H<sub>2</sub> threshold (e.g., McGreer & Bryan 2008; Hirano et al. 2015); the **NGM23** model does not include this effect. These predictions depend on HD chemistry and cooling assumptions (Glover & Abel 2008), and recent work suggests that the abundance of HD cooling halos is likely small ( $\lesssim 10\%$ ; Lenoble et al. 2024). Nonetheless, it will be important to study whether HD cooling impacts the galaxy formation threshold.

Recently, Hicks et al. (2024) found that H<sub>2</sub> cooling is pervasive in their hydrodynamic simulation, even for halos above the H<sub>I</sub> cooling threshold at  $z \gtrsim 12$ . In this work, H<sub>2</sub> cooling is promoted by cold gas flowing into minihalos along filaments, analogous to cold-mode accretion in higher-mass halos (Kereš et al. 2005). Thus, the assumption of virialized gaseous halos—which underlies semi-analytic models for  $M_{\text{crit}}(z)$ —may break down in a cosmological setting, in-

<sup>3</sup> In the absence of radiative feedback and DM–baryon streaming, the H<sub>2</sub> cooling threshold itself differs between these studies due to their respective gas density profile assumptions. This difference does not affect our predictions because we include DM–baryon streaming and LW feedback.

creasing the efficiency of  $H_2$  cooling and potentially alleviating the slight  $f_{\text{gal}}$  tension for MW subhalos that we identify.

Our conclusions are broadly consistent with semi-analytic galaxy formation models. Specifically, our finding that  $H_2$  enables star formation in (sub)halos  $M_{\text{peak}} \lesssim 10^8 M_{\odot}$  agrees with Ahvazi et al. (2024), who modeled  $H_2$  cooling in GALACTICUS. Predictions using GRUMPY in Kravtsov & Manwadkar (2022) and Manwadkar & Kravtsov (2022) also support this result, although these authors populated subhalos slightly below  $M_{\text{peak}} = 10^7 M_{\odot}$ . In addition, Kravtsov & Manwadkar (2022) found that the 50% occupation mass decreases by  $\sim 1$  dex when  $z_{\text{reion}}$  decreases from 9 to 6. Meanwhile, Chen et al. (2022) used A-SLOTH to predict how  $f_{\text{gal}}$  depends on the DM–baryon streaming velocity; their results are consistent with our findings in Appendix A. These authors found that other parameters in A-SLOTH (e.g., the Pop II initial mass function slope) do not affect  $f_{\text{gal}}$ .

The occupation fraction is challenging to predict using cosmological hydrodynamic simulations because it probes galaxy formation over a wide range of spatial and temporal scales. Thus, it is not surprising that  $f_{\text{gal}}$  varies systematically with resolution in hydrodynamic simulations (e.g., Munshi et al. 2021). For example, with a baryonic mass resolution of  $30 M_{\odot}$ , Wheeler et al. (2019) found that *all* halos with  $M(z=0) \gtrsim 4 \times 10^8 M_{\odot}$  form stars. Meanwhile, recent simulations from Gutcke et al. (2022) approach single-star mass resolution and indicate that halos below  $M_{\text{crit}}(z)$  from BF20 form stars, consistent with our results. We caution that—even at such high resolution—sub-grid models for gas evolution and star formation may affect  $f_{\text{gal}}$ .

Looking forward, it is exciting to consider how this work informs searches for the remnants of the first stars (see

Bromm 2013 and Klessen & Glover 2023 for reviews). In particular, our framework predicts the descendant properties of star-forming minihalos in a cosmological setting, including their distribution in the MW (also see Jeon et al. 2017; Rossi et al. 2024; Hartwig et al. 2024). Combining these predictions with stellar evolution models offers a promising avenue to probe the galaxy formation threshold through near-field cosmology, which we look forward to pursuing.

## ACKNOWLEDGMENTS

We are grateful to Niusha Ahvazi for sharing data from Ahvazi et al. (2024), Stacy Kim for encouraging our resimulation, and Viraj Manwadkar for sharing data from Manwadkar & Kravtsov (2022). We thank the referee for constructive feedback, Niusha Ahvazi, Shaun Brown, Viraj Manwadkar, Olof Nebrin, Mike Norman, and Martin Rey for comments on the manuscript, and Andrew Benson, Dusan Kereš, Stacy Kim, and Risa Wechsler for helpful discussions.

The resimulation presented here was conducted through Carnegie’s partnership in the Resnick High Performance Computing Center, a facility supported by Resnick Sustainability Institute at the California Institute of Technology. This work used data from the Milky Way-est suite of simulations, hosted at <https://web.stanford.edu/group/gfc/gfcsims/>, which were supported by the Kavli Institute for Particle Astrophysics and Cosmology at Stanford University, SLAC National Accelerator Laboratory, and the U.S. Department of Energy under contract number DE-AC02-76SF00515 to SLAC National Accelerator Laboratory.

## REFERENCES

- Abel, T., Bryan, G. L., & Norman, M. L. 2002, *Science*, 295, 93
- Ahvazi, N., Benson, A., Sales, L. V., et al. 2024, *MNRAS*, 529, 3387
- Barkana, R. & Loeb, A. 1999, *ApJ*, 523, 54
- Bechtol, K., Birrer, S., Cyr-Racine, F.-Y., et al. 2022, *arXiv e-prints*, arXiv:2203.07354
- Behroozi, P. S., Wechsler, R. H., & Wu, H.-Y. 2013a, *ApJ*, 762, 109
- Behroozi, P. S., Wechsler, R. H., Wu, H.-Y., et al. 2013b, *ApJ*, 763, 18
- Benitez-Llambay, A. & Frenk, C. 2020, *MNRAS*, 498, 4887
- Bromm, V. 2013, *Reports on Progress in Physics*, 76, 112901
- Bryan, G. L. & Norman, M. L. 1998, *ApJ*, 495, 80
- Buch, D., Nadler, E. O., Wechsler, R. H., & Mao, Y.-Y. 2024, *ApJ*, 971, 79
- Chen, L.-H., Magg, M., Hartwig, T., et al. 2022, *MNRAS*, 513, 934
- Correa, C. A., Wyithe, J. S. B., Schaye, J., & Duffy, A. R. 2015, *MNRAS*, 452, 1217
- Diemer, B. & Joyce, M. 2019, *ApJ*, 871, 168
- Drlica-Wagner, A., Bechtol, K., Mau, S., et al. 2020, *ApJ*, 893, 47
- Efstathiou, G. 1992, *MNRAS*, 256, 43P
- Faucher-Giguère, C.-A. 2020, *MNRAS*, 493, 1614
- Fialkov, A., Barkana, R., Tseliakhovich, D., & Hirata, C. M. 2012, *MNRAS*, 424, 1335
- Glover, S. C. O. & Abel, T. 2008, *MNRAS*, 388, 1627
- Graus, A. S., Bullock, J. S., Kelley, T., et al. 2019, *MNRAS*, 488, 4585
- Greif, T. H., Johnson, J. L., Klessen, R. S., & Bromm, V. 2008, *MNRAS*, 387, 1021
- Gutcke, T. A., Pfrommer, C., Bryan, G. L., et al. 2022, *ApJ*, 941, 120
- Hahn, O. & Abel, T. 2011, *MNRAS*, 415, 2101
- Haiman, Z., Rees, M. J., & Loeb, A. 1996, *ApJ*, 467, 522
- Haiman, Z., Rees, M. J., & Loeb, A. 1997, *ApJ*, 476, 458
- Hartwig, T., Lipatova, V., Glover, S. C. O., & Klessen, R. S. 2024, *MNRAS*, 535, 516
- Hegde, S. & Furlanetto, S. R. 2023, *MNRAS*, 525, 428
- Hicks, W. M., Norman, M. L., Wells, A. I., & Bordner, J. O. 2024, *arXiv e-prints*, arXiv:2407.20429

- Hicks, W. M., Wells, A., Norman, M. L., et al. 2021, *ApJ*, 909, 70
- Hinshaw, G., Larson, D., Komatsu, E., et al. 2013, *ApJS*, 208, 19
- Hirano, S., Hosokawa, T., Yoshida, N., Omukai, K., & Yorke, H. W. 2015, *MNRAS*, 448, 568
- Incatasciato, A., Khochfar, S., & Oñorbe, J. 2023, *MNRAS*, 522, 330
- Ivezić, Ž., Kahn, S. M., Tyson, J. A., et al. 2019, *ApJ*, 873, 111
- Jaacks, J., Finkelstein, S. L., & Bromm, V. 2019, *MNRAS*, 488, 2202
- Jeon, M., Besla, G., & Bromm, V. 2017, *ApJ*, 848, 85
- Kazuno, Y., Mori, M., Kaneda, Y., & Otaki, K. 2024, *PASJ*, 76, L39
- Kereš, D., Katz, N., Weinberg, D. H., & Davé, R. 2005, *MNRAS*, 363, 2
- Klessen, R. S. & Glover, S. C. O. 2023, *ARA&A*, 61, 65
- Kravtsov, A. & Manwadkar, V. 2022, *MNRAS*, 514, 2667
- Kulkarni, M., Visbal, E., & Bryan, G. L. 2021, *ApJ*, 917, 40
- Lenoble, R., Commerçon, B., & Rosdahl, J. 2024, *A&A*, 685, A7
- Liu, B. & Bromm, V. 2020, *MNRAS*, 497, 2839
- Machacek, M. E., Bryan, G. L., & Abel, T. 2001, *ApJ*, 548, 509
- Manwadkar, V. & Kravtsov, A. V. 2022, *MNRAS*, 516, 3944
- McGreer, I. D. & Bryan, G. L. 2008, *ApJ*, 685, 8
- Munshi, F., Brooks, A. M., Applebaum, E., et al. 2021, *ApJ*, 923, 35
- Nadler, E. O., Gluscevic, V., Driskell, T., et al. 2024, *ApJ*, 967, 61
- Nadler, E. O., Wechsler, R. H., Bechtol, K., et al. 2020, *ApJ*, 893, 48
- Nadler, E. O., Mansfield, P., Wang, Y., et al. 2023, *ApJ*, 945, 159
- Nebrin, O., Giri, S. K., & Mellema, G. 2023, *MNRAS*, 524, 2290
- Norman, M. L., Chen, P., Wise, J. H., & Xu, H. 2018, *ApJ*, 867, 27
- Oh, S. P. & Haiman, Z. 2002, *ApJ*, 569, 558
- O’Shea, B. W. & Norman, M. L. 2008, *ApJ*, 673, 14
- Robertson, B. E. 2022, *ARA&A*, 60, 121
- Rossi, M., Salvadori, S., Skúladóttir, Á., Vanni, I., & Koutsouridou, I. 2024, *arXiv e-prints*, arXiv:2406.12960
- Schauer, A. T. P., Glover, S. C. O., Klessen, R. S., & Ceverino, D. 2019, *MNRAS*, 484, 3510
- Schauer, A. T. P., Glover, S. C. O., Klessen, R. S., & Clark, P. 2021, *MNRAS*, 507, 1775
- Skinner, D. & Wise, J. H. 2020, *MNRAS*, 492, 4386
- Tegmark, M., Silk, J., Rees, M. J., et al. 1997, *ApJ*, 474, 1
- Tseliakhovich, D. & Hirata, C. 2010, *PhRvD*, 82, 083520
- Uysal, B. & Hartwig, T. 2023, *MNRAS*, 520, 3229
- van den Bosch, F. C., Jiang, F., Hearin, A., et al. 2014, *MNRAS*, 445, 1713
- Vegetti, S., Birrer, S., Despali, G., et al. 2023, *arXiv e-prints*, arXiv:2306.11781
- Wechsler, R. H., Bullock, J. S., Primack, J. R., Kravtsov, A. V., & Dekel, A. 2002, *ApJ*, 568, 52
- Wheeler, C., Hopkins, P. F., Pace, A. B., et al. 2019, *MNRAS*, 490, 4447
- Wise, J. H. & Abel, T. 2007, *ApJ*, 671, 1559
- Wise, J. H., Demchenko, V. G., Halicek, M. T., et al. 2014, *MNRAS*, 442, 2560
- Wise, J. H., Turk, M. J., Norman, M. L., & Abel, T. 2012, *ApJ*, 745, 50

## APPENDIX

## A. DARK MATTER–BARYON STREAMING

Our fiducial results using the **NGM23** model for  $M_{\text{crit}}(z)$  assume  $v_{\text{str}}(z) = \sigma_{\text{str}}(z)$ . The left panel of Figure 4 shows corresponding  $M_{\text{crit}}(z)$  models with  $v_{\text{str}}(z) = 0$  (dashed) and  $v_{\text{str}}(z) = 2\sigma_{\text{str}}(z)$  (dot-dashed). As discussed in **NGM23**, increasing  $v_{\text{str}}(z)$  raises  $M_{\text{crit}}(z)$ , since it allows baryons to stream out of DM potentials and suppresses gas accretion rates. Decreasing  $v_{\text{str}}(z)$  has the opposite effect.

The right panel of Figure 4 shows our  $f_{\text{gal}}$  predictions for these models, generated using analytic MAHs. For reference, our fiducial results assuming  $v_{\text{str}}(z) = \sigma_{\text{str}}(z)$  are shown by thick, solid lines for  $z_o = 1$  (purple) and  $z_o = 0$  (blue). The magnitude of  $v_{\text{str}}(z)$  clearly affects the  $f_{\text{gal}}$  predictions, such that lower-mass halos are occupied for smaller  $v_{\text{str}}(z)$ . However, these shifts are fairly small compared to the difference between the  $z_o = 1$  and  $z_o = 0$  results, and the slope of  $f_{\text{gal}}$  is not significantly affected by variations in  $v_{\text{str}}(z)$ .

## B. MASS–CONCENTRATION RELATION SCATTER

Our fiducial results assume  $\sigma_{\log(c)} = 0.16$  dex, following the Diemer & Joyce (2019) mass–concentration relation. Here, we consider how varying  $\sigma_{\log(c)}$ , as a proxy for scatter in the underlying distribution of halo MAHs, affects  $f_{\text{gal}}$  predictions. Figure 5 shows the results of this exercise using the analytic MAH model with  $z_o = 1$  (light blue) and  $z_o = 0$  (dark blue), for  $\sigma_{\log(c)} = 0.06$  dex (dashed),  $\sigma_{\log(c)} = 0.16$  dex (solid), and  $\sigma_{\log(c)} = 0.26$  dex (dot-dashed).

The mass at which  $f_{\text{gal}} = 50\%$  is nearly unchanged in all cases, and the  $f_{\text{gal}}$  cutoff becomes steeper as  $\sigma_{\log(c)}$  decreases. This follows because, in the limit  $\sigma_{\log(c)} \rightarrow 0$ , MAHs become deterministic and  $f_{\text{gal}}$  approaches a step function at a mass determined by Equation 1 and  $M_{\text{crit}}(z)$ . We derive this dependence on  $\sigma_{\log(c)}$  in Appendix C.

## C. OCCUPATION FRACTION DERIVATION

Suppose that a halo with mass  $M_o$  at redshift  $z_o$  must exceed a critical mass  $M_*$  at redshift  $z_* > z_o$  to form stars. Under this assumption, Equation 2 can be rewritten as

$$f_{\text{gal}}(M_o, z_o) = p(M(z_*) | M_o, z_o) > M_*). \quad (\text{C1})$$

For  $M_o < M_*$ ,  $f_{\text{gal}} = 0$  for MAHs that strictly increase with time, as in our isolated halo MAH model. For  $M_o > M_*$ , inserting Equation 1 into Equation C1 and rearranging yields

$$f_{\text{gal}}(M_o, z_o) = p\left(\log(c_o) > \log\left[\frac{Sc_1}{\ln(M_o/M_*)} \frac{z_* - z_o}{(1 + z_o)^2}\right]\right), \quad (\text{C2})$$

Since  $\log(c_o)$  is normally distributed, the cumulative distribution in Equation C2 can be rewritten as

$$f_{\text{gal}}(M_o, z_o) = \frac{1}{2} \left[ 1 + \text{erf}\left(\frac{\mu_{\log(c)}(z_o) - \log(c_*)}{\sqrt{2}\sigma_{\log(c)}}\right) \right], \quad (\text{C3})$$

where  $\mu_{\log(c)}$  is the mean of the Diemer & Joyce (2019) mass–concentration relation and  $c_*$  is the value of  $c_o$  that saturates the inequality in Equation C2.

This derivation shows that the mass–concentration relation scatter sets the slope of  $f_{\text{gal}}$ , while its amplitude sets the cutoff scale. In particular,  $f_{\text{gal}}$  becomes steeper as  $\sigma_{\log(c)}$  decreases and approaches a step function as  $\sigma_{\log(c)} \rightarrow 0$ , consistent with our results in Appendix B. Equation C3 matches our fiducial results reasonably well when  $z_*$  is chosen to be the lowest redshift that affects  $f_{\text{gal}}$  in a given model (e.g., for  $z_* = 10$  and  $M_* = 2 \times 10^7$  and  $5 \times 10^7 M_\odot$  for the **NGM23** and **BF20** models, respectively). A more accurate analytic model would require integrating over redshift rather than assuming  $f_{\text{gal}}$  is determined at  $z_*$ .

Equation C3 is similar to the form of  $f_{\text{gal}}$  used in previous work (e.g., Graus et al. 2019; Nadler et al. 2020),

$$f_{\text{gal}}(M_{\text{peak}}) = \frac{1}{2} \left[ 1 + \text{erf}\left(\frac{\log(M_{\text{peak}}/M_\odot) - \mathcal{M}_{50}}{\sqrt{2}\sigma_{\text{gal}}}\right) \right], \quad (\text{C4})$$

where  $f_{\text{gal}}(\mathcal{M}_{50}) \equiv 0.5$ . We leave a study of the correspondence between these expressions to future work.

## D. CONVERGENCE TEST

Figure 6 compares our fiducial  $f_{\text{gal}}$  prediction for MW subhalos to a lower-resolution (LR) simulation of the same host, run with a particle mass of  $5 \times 10^4 M_\odot$  and softening length of  $80 \text{ pc } h^{-1}$ , originally presented in Buch et al. (2024). For the LR simulation, we apply a 300-particle cut at  $z = 0$  corresponding to  $M_{\text{vir}} > 1.5 \times 10^7 M_\odot$ . The LR prediction is consistent with our fiducial result within the bootstrap uncertainties for  $M_{\text{peak}} \gtrsim 1.5 \times 10^7 M_\odot$ , while the high-resolution simulation resolves star formation in lower- $M_{\text{peak}}$  subhalos when using the **NGM23** model.<sup>4</sup> We predict slightly higher  $f_{\text{gal}}$  in the LR simulation for  $10^8 \lesssim M_{\text{peak}}/M_\odot \lesssim 10^{8.5}$ , which may result from noisy  $M_{\text{peak}}$  measurements at high redshifts in the LR simulation. Nonetheless, our  $f_{\text{gal}}$  predictions are not very sensitive to resolution down to the 300-particle limit imposed throughout our analyses.

## E. HOST-TO-HOST SCATTER

Here, we compare  $f_{\text{gal}}$  predictions for MW subhalos using several zoom-ins at a resolution lower than our fiducial resimulation. This comparison is meant to assess host-to-host scatter in  $f_{\text{gal}}$  and does not supersede our fiducial high-resolution result. Specifically, we compare  $f_{\text{gal}}$  predicted using the LR resimulation of Halo004 from Appendix D to the Halo416 simulation at the same resolution from Nadler

<sup>4</sup> In the **NGM23** case, the downturn in the LR  $f_{\text{gal}}$  result at high  $M_{\text{peak}}$  results from the slight increase in  $M_{\text{crit}}(z)$  from **NGM23** relative to **BF20** near  $z_{\text{reion}}$ . However, this downturn is not statistically significant.



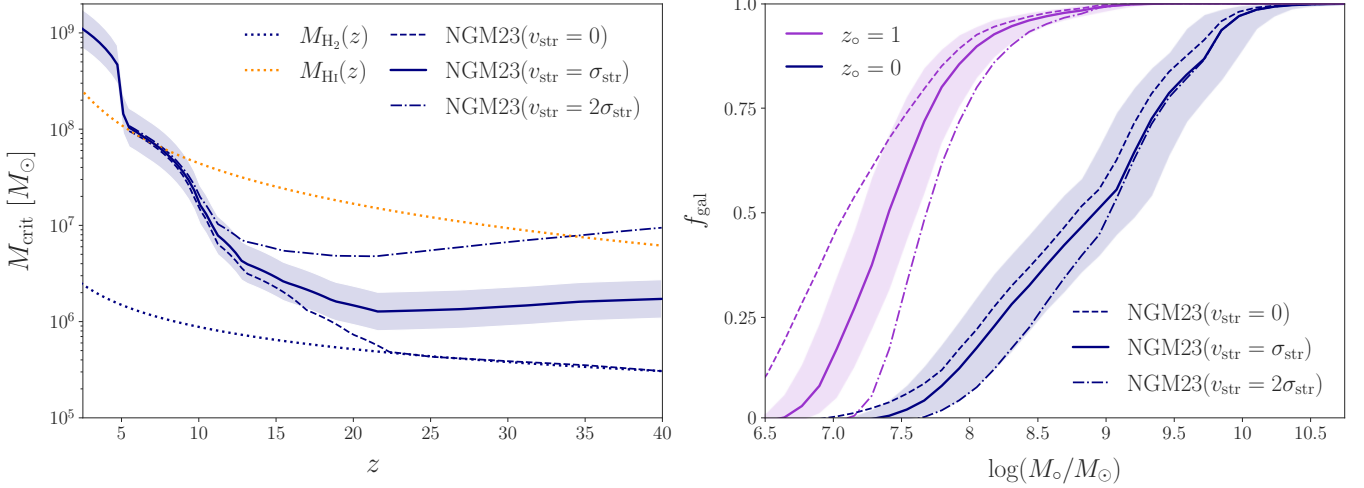


**Figure 4.** *Left:* Halo mass thresholds for star formation, showing versions of the NGM23 model with  $v_{\text{str}} = 0$  (dashed),  $v_{\text{str}} = \sigma_{\text{str}}$  (solid; our fiducial choice), and  $v_{\text{str}} = 2\sigma_{\text{str}}$  (dot-dashed). We only show  $M_{\text{crit}}(z)$  scatter for the  $v_{\text{str}} = \sigma_{\text{str}}$  case for clarity, but we marginalize over this scatter in all cases. *Right:* Median galaxy occupation fraction for isolated halos, predicted by combining analytic MAHs with the models in the left panel, with  $z_0 = 1$  (purple) and  $z_0 = 0$  (blue). Shaded bands show 16% to 84% intrinsic scatter quantiles for the  $v_{\text{str}} = \sigma_{\text{str}}$  cases.

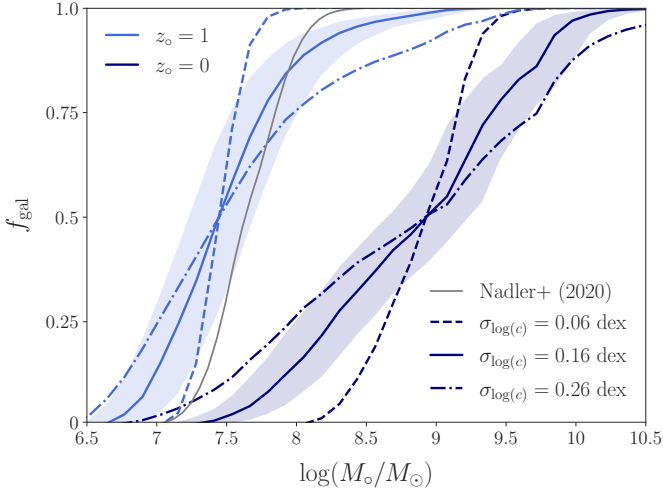


**Figure 5.** Median galaxy occupation fraction for isolated halos, predicted by combining analytic MAHs with our fiducial NGM23  $M_{\text{crit}}(z)$  model, for  $z_0 = 1$  (light blue) and  $z_0 = 0$  (dark blue). Predictions are generated using  $\sigma_{\log(c)} = 0.06$  dex (dashed),  $\sigma_{\log(c)} = 0.16$  dex (solid; our fiducial choice), and  $\sigma_{\log(c)} = 0.26$  dex (dot-dashed). The thin gray line shows the best-fit model from Nadler et al. (2020), for reference. Shaded bands show 16% to 84% intrinsic scatter quantiles for the  $\sigma_{\log(c)} = 0.16$  dex cases; we marginalize over this scatter in all cases.

et al. (2020).<sup>5</sup> We also compare the LX14 Caterpillar-4 and Caterpillar-53 simulations analyzed in Manwadkar & Kravtsov (2022), which were run with a particle mass of

<sup>5</sup> The main analyses in Nadler et al. (2020) use an even lower-resolution version of Halo416, although they show that their main results converge when using the LR Halo416 run we consider here.

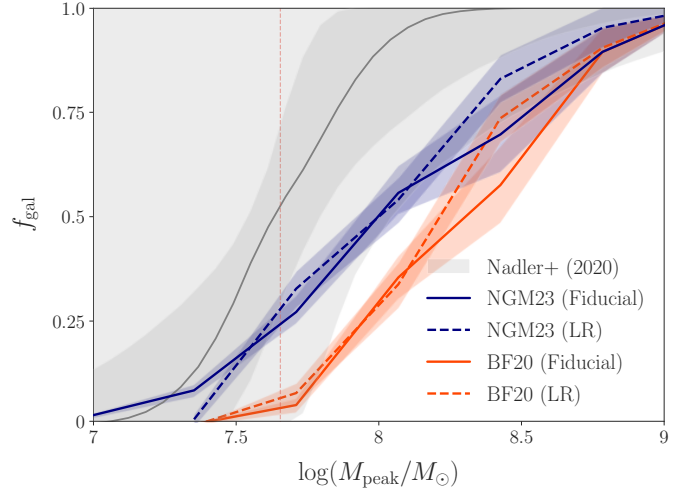


**Figure 6.** Comparison between our fiducial simulation predictions for  $f_{\text{gal}}$  ( $m_{\text{particle}} = 6.3 \times 10^3 M_{\odot}$ ; solid) to a simulation of the same host at lower resolution (LR;  $m_{\text{particle}} = 5 \times 10^4 M_{\odot}$ ; dashed). Results using the NGM23 model are shown in blue, and results using the BF20 model with  $z_{\text{reion}} = 7$  are shown in orange. Shaded bands show 16% to 84% quantiles from bootstrap resampling. The gray shaded region shows the Nadler et al. (2020) posterior, as in Figure 3.

$3 \times 10^4 M_{\odot}$  and a softening of  $76 \text{ pc } h^{-1}$ , comparable to our Halo004 and Halo416 LR runs. Note that all four simulations we compare contain realistic LMC analogs. We apply a 300-particle cut on  $M(z=0)$  in each case, and we use the BF20 model since the  $f_{\text{gal}}$  cutoff converges at low resolution in this case, according to Appendix D.

Figure 7 compares the resulting  $f_{\text{gal}}$  predictions. The Halo416 and Caterpillar occupation fractions are consistent with our Halo004 LR results when using the BF20 model. In detail, slightly lower-mass halos are populated

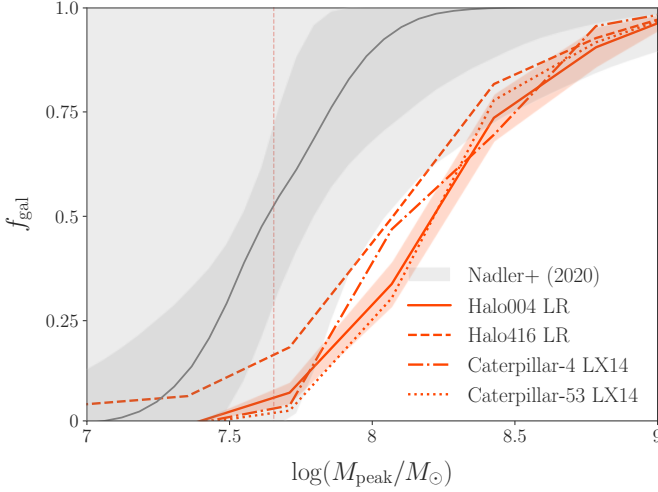


**Figure 7.** Comparison between  $f_{\text{gal}}$  predictions for the host used in this work (Halo004, solid), the host used in Nadler et al. (2020) (Halo416, dashed), and the hosts used in Manwadkar & Kravtsov (2022) (Caterpillar-4, dash-dotted, and Caterpillar-53, dotted). Halo004 and Halo416 are shown at the “low resolution” described in Appendix D, which is comparable to the LX14 resolution of the Caterpillar hosts. Results are only shown for the BF20 model (orange). The orange shaded bands shows 16% to 84% quantiles from bootstrap resampling the Halo004 LR result. The gray shaded region shows the Nadler et al. (2020) posterior, as in Figure 3.

in Caterpillar-4 and Halo416 compared to Halo004. For Halo416, this shifts  $f_{\text{gal}}$  toward the Nadler et al. (2020) posterior by an amount comparable to the bootstrap uncertainty on our Halo004 result. For all hosts except Halo416, virtually no halos with  $M_{\text{peak}} \approx 10^{7.5} M_{\odot}$  form stars in the BF20 case. When using the NGM23 model, the host-to-host scatter in  $f_{\text{gal}}$  increases in this case, which is likely a result of poorly-resolved subhalo MAHs near the  $f_{\text{gal}}$  cutoff. We conclude that host-to-host scatter does not significantly affect our main conclusions, although it can ease the tension between our fiducial  $f_{\text{gal}}$  predictions and MW satellite constraints.